THE JOURNAL OF PHYSICAL CHEMISTRY C

Article

pubs.acs.org/JPCC

Core–Shell Structure of Palladium Hydride Nanoparticles Revealed by Combined X-ray Absorption Spectroscopy and X-ray Diffraction

Aram L. Bugaev,[*,†,‡] Alexander A. Guda,[†] Kirill A. Lomachenko,[†,§] Viktor V. Shapovalov,[†] Andrea Lazzarini,[‡,∥] Jenny G. Vitillo,[‡] Lusegen A. Bugaev,[†] Elena Groppo,[‡] Riccardo Pellegrini,[⊥] Alexander V. Soldatov,[†] Jeroen A. van Bokhoven,[#,○] and Carlo Lamberti[*,†,‡]

[†]The Smart Materials Research Centre, Southern Federal University, Sladkova 174/28, 344090 Rostov-on-Don, Russia

[‡]Department of Chemistry, NIS and CrisDi Interdepartmental Centres, asn INST Reference Center, University of Turin, Via P. Giuria 7, 10125 Turin, Italy

[§]European Synchrotron Radiation Facility, 71 avenue des Martyrs, CS 40220, 38043 Grenoble Cedex 9, France

[∥]inGAP Centre for Research Based Innovation, Department of Chemistry, University of Oslo, P.O. Box 1033, N-0315 Oslo, Norway

[⊥]Catalyst Division, Chimet SpA, Via di Pescaiola 74, 52041 Viciomaggio Arezzo, Italy

[#]Institute for Chemical and Bioengineering, ETH Zurich, Vladimir-Prelog-Weg 1, 8093 Zurich, Switzerland

[○]Laboratory for Catalysis and Sustainable Chemistry, Paul Scherrer Institute, 5232 Villigen, Switzerland

Supporting Information

ABSTRACT: We report an in situ, temperature and H_2 pressure-dependent, characterization of (2.6 ± 0.4) nm palladium nanoparticles supported on active carbon during the process of hydride phase formation. For the first time the core–shell structure is highlighted in the single-component particles on the basis of a different atomic structure and electronic configurations in the inner "core" and surface "shell" regions. The atomic structure of these particles is examined by combined X-ray powder diffraction (XRPD), which is sensitive to the crystalline core region of the nanoparticles, and by first shell analysis of extended X-ray absorption fine structure (EXAFS) spectra, which reflects the averaged structure of both the core and the more disordered shell. In the whole temperature range (0–85 °C), XRPD analysis confirms the existence of two well-separated α- and β-hydride phases with the characteristic flat plateau in the phase transition region of the pressure-lattice parameter isotherms. In contrast, first shell interatomic distances obtained from EXAFS exhibit a slope in the phase transition region, typical for nanostructured palladium. Such difference is explained by distinct properties of bulk "core" which has crystalline structure and sharp phase transition, and surface "shell" which is amorphous and absorbs hydrogen gradually without forming distinguishable α- and β-phases. Combining EXAFS and XRPD we extract, for the first time, the Pd–Pd first-shell distance in the amorphous shell of the nanoparticles, that is significantly shorter than in the bulk core and relevant in catalysis. The core/shell model is supported by the EXAFS analysis of the higher shells, in the frame of the multiple scattering theory, showing that the evolution of the third shell distance ($\Delta R_3/R_3$) is comparable to the evolution of ($\Delta a/a$) obtained from XRPD since amorphous PdH_x shell gives a negligible contribution in this range of distances. This operando structural information is relevant for the understanding of structure-sensitive reactions. Additionally, we demonstrate the differences in the evolution of the thermal parameters obtained from EXAFS and XRPD along the hydride phase formation.

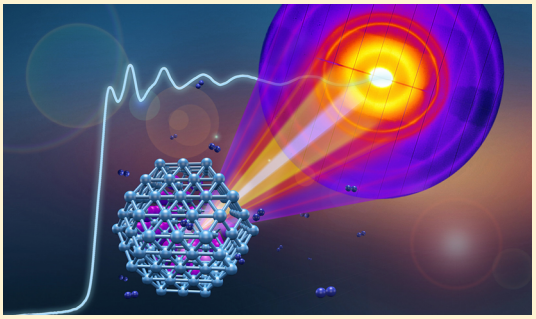

1. INTRODUCTION

Palladium-based nanomaterials are extensively used as catalysts,[1−17] sensors,[18,19] and biosensors,[20−24] and in electrochemistry.[21,25] In a number of industrial applications, supported palladium nanoparticles are used to catalyze hydrogenation reactions.[26−34] In the presence of hydrogen, they form different types of hydrides,[35−48] whose relative abundance affects the catalytic performances, especially in terms of selectivity.[31,49,50] Therefore, understanding the structure of palladium hydride phases and building an atomistic model of hydride phase formation in palladium nanoparticles is a problem of high scientific interest and industrial relevance.

Bulk palladium exhibits two hydride phases depending on the stoichiometric atomic ratio x of the PdH_x.[51] The region $0 < x \leq 0.03$ corresponds to the α-phase, while in the region of $x \geq 0.58$ the β-phase is formed. The coexistence of these phases is observed in the region from 0.03 to 0.58. Formation of the

Received: May 2, 2017
Revised: June 17, 2017
Published: June 20, 2017

DOI: 10.1021/acs.jpcc.7b04152
J. Phys. Chem. C XXXX, XXX, XXX−XXX

hydride phase does not change the symmetry of the initial face centered cubic lattice of the palladium bulk, but leads to an increase of the cell parameter. The latter has a stepwise behavior at the concentrations corresponding to the formation of α- and β-phases, while within each of the phases it linearly increases with x. Palladium nanoparticles are expected to show different thermodynamics of hydrogen absorption in comparison to bulk materials due to a considerable contribution of the surface.[40,52] Phase separation was also observed in palladium particles down to nanometer size,[53,54] but the relationship between H_2 equilibrium pressure (P_{H_2}) and x loading differs from bulk and strongly depends on the size and shape of the nanoparticles.[39] This affects the maximum x loading of hydrogen in the β-phase, and the extension of the plateau between α- and β-phases.

In the present work, we focus on the process of hydride phase formation in carbon-supported palladium nanoparticles (average particle size of 2.6 nm, with 0.4 nm in standard deviation) as a function of temperature (0−85 °C) and P_{H_2} (0−1000 mbar), by coupling simultaneous X-ray powder diffraction (XRPD) and extended X-ray absorption fine structure spectroscopy (EXAFS) experiments with independent volumetric measurements. XRPD allows monitoring the increase of the cell parameter a during the hydride formation, differentiating between the α- and β- hydride phases, but it is scarcely informative for nanoparticles with sizes below 1 nm[53,54] (that do not contribute to the Bragg reflections) and to the external shell of nanoparticles (because of disorder effects intrinsic in surface layers). Being element specific, EXAFS selectively probes the local environment around the Pd absorbing atom, yielding average Pd−Pd interatomic distances, coordination numbers, and Debye−Waller parameters and providing important complementary information on the surface of the nanoparticles,[55−67] which is merged with the information on the core. Finally, volumetric measurements[68,69] provide quantitative information on the amount of hydrogen absorbed in terms of the average H/Pd atomic ratio, provided that the hydrogen uptake from the support is properly taken into account.

The synergic coupling of the three techniques highlighted clear differences in the structural configuration of the palladium atoms in the shell and in the core of the nanoparticles during the Pd ↔ PdH_x phase transition. In particular, XRPD revealed the subsequent formation of two well-separated α- and β-hydride phases with a a flat plateau, similar to that obtained for bulk Pd. In contrast, the contribution of the surface to the first shell EXAFS analysis[70] resulted in a smoother evolution of the Pd−Pd first shell interatomic distance, which evidences the presence of a core−shell structure in the PdH_x nanoparticles. Unlike the previously reported independent XRPD and first shell EXAFS study,[71] performed on similar sized Pd nanoparticles (2.5 ± 0.5 nm) and reporting only the starting (Pd) and final ($PdH_{0.4}$) points of the of the PdH_x system at ambient temperature, we collected more than hundred points in the P_{H_2}-temperature plane by simultaneous XRPD and EXAFS data collection (the latter analyzed until the fourth shell), which was a crucial step to highlight the core−shell structure. We have also observed a different behavior of the Debye−Waller parameter in EXAFS and isotropic atomic displacement in XRPD fits, which is explained by the fundamental difference of the two methods.

2. MATERIALS, EXPERIMENTS, AND METHODS

2.1. Sample Preparation and Characterization. Five wt % Pd on carbon catalyst supplied by Chimet S.p.A. has been prepared by deposition−precipitation method[72] on activated carbon of wood origin (surface area = 980 $m^2\ g^{-1}$; pore volume = 0.62 $cm^3\ g^{-1}$).[73,74] A palladium black sample has been prepared following a procedure similar to that adopted for the catalyst preparation, but omitting the support, and successively reduced in H_2 at 120 °C, resulting in a stable bulk Pd^0 phase.

2.2. In Situ X-ray Absorption Spectroscopy and X-ray Powder Diffraction Setup. Pd K-edge X-ray absorption spectroscopy and X-ray powder diffraction data were collected at the BM01B[75,76] (Swiss-Norwegian Beamline, successively moved to the BM31 port) of the European Synchrotron Radiation Facility (ESRF), Grenoble, France. The beamline allows a rapid (about 30 s) plug and play switch between X-ray absorption and X-ray diffraction setups, allowing to measure for each of the selected P_{H_2}-temperature conditions, both EXAFS and XRPD on exactly the same point of the PdH_x phase diagram. A boron glass capillary 1.0 mm in diameter filled with the sample powder was connected to a remotely controlled gas rig enabling to vary the P_{H_2} during the experiment. Vacuum pump was connected to the system for outgassing, providing a minimal pressure lower than 0.1 mbar. Nitrogen-based gas blower positioned above the sample allowed to control the temperature from values below 0 °C and up to 150 °C. To remove the surface oxide layer formed on the palladium nanoparticles exposed to air,[77] initial pretreatment of the sample was performed at 125 °C in 200 mbar of hydrogen for 30 min. EXAFS/XRPD data were collected at five different temperatures from 0 to 85 °C increasing the pressure from 0 to 1000 mbar. Since the temperatures of the gas blower set-point may differ from the real temperature of the catalyst, we report the temperatures of the samples. These temperatures were obtained by matching the pressures of the phase transition to the corresponding point of the Van 't Hoff plot, derived from the volumetric measurements of this sample (see section 2.3 below and section S4 and Figure S10 of the Supporting Information). The pressure always corresponds to the absolute hydrogen pressure, which was the only gas used. The pressure steps were chosen in the way to have more experimental points in the region of α- to β-phase transition. To completely remove the hydrogen loaded in the sample during the previous isotherm, the sample was outgassed in vacuum for 30 min at 125 °C before each measurement.

X-ray absorption spectra at the Pd K-edge were obtained in the transmission mode by continuous scanning of the double crystal Si(111) monochromator from 24.1 to 25.4 keV, taking 5 min per spectrum. Palladium foil was measured simultaneously with each spectrum for energy calibration using a third ionization chamber. Palladium black powder was used as a reference sample. X-ray powder diffraction was measured using 0.50544(2) Å radiation, selected by a Si(111) channel-cut monochromator. CMOS-Dexela 2D detector positioned at the distance of 250.24(7) mm from the sample resulted in a 2θ range from 2 to 52 degrees (d_{min} = 0.58 Å). The values of the photon wavelength, sample to detector distance and detectors tilts have been optimized by Rietveld refinement of NIST LaB_6 and Si samples and kept fixed in the refinement of the Pd/C samples. For better statistics 20 diffraction images and 20 dark images (without X-ray beam) with acquisition time of 5 s were collected at each experimental point.

DOI: 10.1021/acs.jpcc.7b04152
J. Phys. Chem. C XXXX, XXX, XXX−XXX

X-ray absorption spectra were analyzed in Demeter 0.9.21 package[78] including background subtraction, normalization, energy calibration, and single-shell Fourier analysis. A real space data fitting in the R-range from 1.5 to 3.2 Å was performed to the Fourier-transformed k^2-weighted data in the k-range from 5 to 12 Å^{-1}, corresponding to the number of independent points $2\Delta k\Delta R/\pi > 7$. The low k-region (2−5 Å^{-1}) was intentionally excluded from the analysis to minimize the Pd−C contribution from interaction of the nanoparticles with the support. The fit included four parameters: the first shell Pd−Pd interatomic distance (R_1), the Debye−Waller factor (σ^2), energy shift (ΔE_0) and coordination number (N). The parameters ΔE_0 and N were considered as common variables for all spectra. The value of the passive electron reduction factor $S_0^2 = 0.83 \pm 0.03$ was obtained by fitting the spectrum of palladium foil and kept constant in the optimization of all the spectra collected on the Pd-catalyst. For higher-shell analysis (section 4.3) the R-range from 1.2 to 5.5 Å and k-range from 3.0 to 14.0 Å^{-1} were used ($2\Delta k\Delta R/\pi > 30$). In the fits S_0^2 was fixed to 0.83 and a single ΔE_0 was optimized for all single scattering (SS) and multiple scattering paths; four independent R_1, R_2, R_3, and R_4 distances were optimized for the four SS paths, with four independent (σ_i^2) parameters, resulting in nine independent parameters. The coordination numbers of the first four shells in the nanoparticles have been fixed to the size-dependent values given by the model developed by Calvin et al.,[79] see below eq 3. To minimize the number of optimized parameters, guaranteeing stability to the fits, for all relevant MS paths, the path length and the corresponding σ^2 parameter were constrained by the values of R_i and σ_i^2 as already successfully done in other studies.[80−82] For both first shell and higher shells analyses, the fitting was performed in R-space using theoretical amplitudes and phases calculated by FEFF6 code.[83]

2D XRPD patterns were processed by PyFAI[84] software which executes fast averaging, background subtraction and integrating of images to obtain I(2θ) patterns. Rietveld refinement was performed in Jana2006 code.[85] Profile parameters were optimized by fitting the diffraction patterns of bare and the most hydrogenated samples at each temperature. In the final refinement, we optimized the fractions of α and β phases and the cell parameters corresponding to each phase.

2.3. Volumetric Measurements. Hydrogen sorption isotherms were measured on a commercial volumetric apparatus (Micromeritics ASAP2020). The instrument was equipped with four pressure transducers, allowing us to investigate the sorption process at very low equilibrium pressures (down to 10^{-4} mbar). Prior to the measurements, the Pd/C powders (1.4 g) were activated on a vacuum line equipped with a turbomolecular pump ($P < 10^{-4}$ mbar): after degassing at 120 °C for 3 h, the sample was subjected to two H_2 absorption/desorption cycles at 120 °C in hydrogen (absorption pressure, ∼100 mbar; desorption pressure, dynamic vacuum) to guarantee a full reduction of the palladium nanoparticles. Then the sample was exposed to 100 mbar of H_2 and cooled down to room temperature. The sample was successively transferred inside a glovebox (M Braun Lab Star glove box supplied with pure 5.5 grade N_2, < 0.5 ppm of O_2, < 0.5 ppm of H_2O) before being inserted into the measurement cell and degassed at room temperature for 1 h on the volumetric apparatus. The H_2 uptake of the (Pd-free) carbon support was measured in the same conditions adopted for the Pd/C catalyst, after activation in dynamic vacuum at 120 °C overnight. Hydrogen gas (99.9999 vol % purity) was supplied by Rivoira SpA. The isotherms reported in the following for the Pd/C systems were obtained from the measured ones after the subtraction of the H_2 uptake measured under the same conditions for the activated carbon support (see Supporting Information).

3. RESULTS

The narrow particle size distribution of the nanoparticles is a fundamental prerequisite for extracting reliable information from both XRPD and EXAFS data. Therefore, the Pd/C catalyst was initially investigated by means of high resolution transmission electron microscope (HRTEM: JEOL 3010-UHR instrument operating at 300 kV and equipped with a 2k × 2k pixels Gatan US1000 CCD camera), to determine in a direct way the average particle size and the particle size distribution. A representative TEM micrograph is reported in Figure 1, where

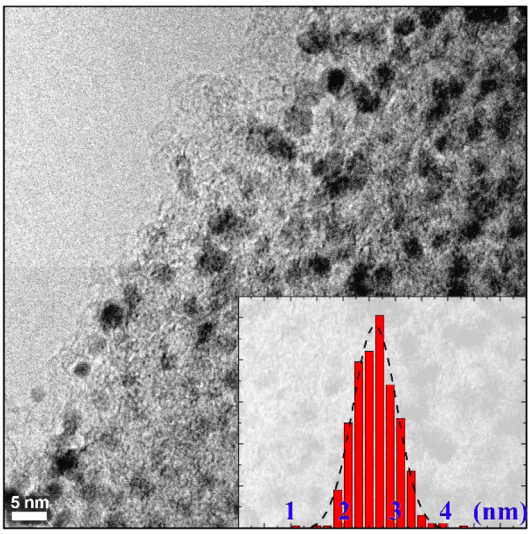

Figure 1. Representative TEM micrograph of the Pd/C sample and corresponding particle size distribution.

the palladium particles appear homogeneously distributed on the carbon support in an isolated form without aggregates. A careful analysis of several TEM images containing more than 500 independent particles revealed that the average size of the palladium particles is 2.6 ± 0.4 nm.

In a second step, the formation of the palladium hydride phase as a function of the hydrogen pressure and temperature was investigated by coupling synchrotron EXAFS and XRPD experiments (Figure 2) with volumetric measurements (see sections S2−S4 of the Supporting Information for details in the data collection), obtained almost simultaneously. The progressive formation of the Pd-hydride phase upon increasing P_{H_2} at constant temperature leads to the expansion of the palladium lattice (i.e., the increase of the first shell Pd−Pd interatomic distance), because of the insertion of hydrogen in the octahedral interstitial positions. The increase of the first shell Pd−Pd interatomic distances is observed in the Fourier-transforms of the Pd K-edge EXAFS spectra (Figure 2a) and leads to a shift of the XRPD reflections toward smaller 2θ angles (Figure 2b).

The whole set of EXAFS data shown in Figure 2a was analyzed with a first-shell Fourier approach (section S2). The Pd−Pd distance was found to change along each isotherm as a

DOI: 10.1021/acs.jpcc.7b04152
J. Phys. Chem. C XXXX, XXX, XXX−XXX

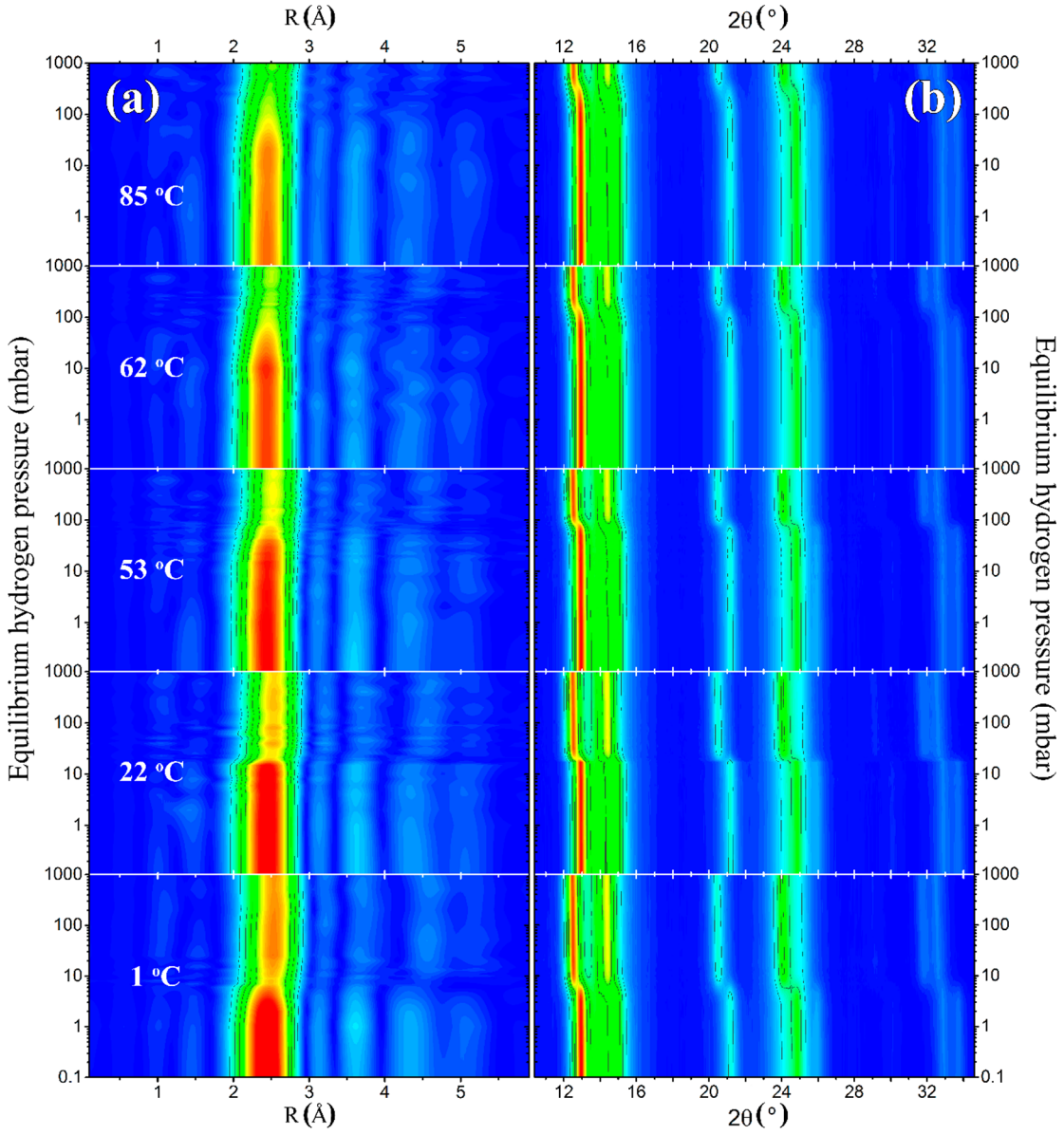

Figure 2. Evolution of the k^2-weighted, phase uncorrected Fourier-transformed EXAFS data $|\chi(R)|$ (part a), and XRPD patterns (part b) during the palladium hydride formation at different temperatures. For all FT-EXAFS spectra the same color scale has been adopted, which allows to appreciate the intensity reduction of the first shell Pd−Pd contribution (2−3 Å range) due to structural (PdH_x formation) and thermal disorder. Each XRPD pattern has been normalized to its total scattering area.

function of P_{H_2}. The resulting palladium hydride pressure-distance curves are shown in Figure 3a. It is worth noticing that the lattice expansion process is accompanied by an increase in the Debye−Waller parameter, σ^2, which will be discussed in section 4.4.

In contrast to EXAFS, XRPD is a phase-specific technique. Hence, it enables to analyze separately the α- and β- hydride phases present in the sample at each point of the isotherm. The relative concentrations of the α- and β-phases and the cell parameters within each phase have been determined by a 2-phases Rietveld refinement procedure (see section S3 of the Supporting Information). To plot the structural isotherms obtained from XRPD in a way directly comparable with the EXAFS data (Figure 3a), we calculated the averaged cell parameter as a weighted sum

$$a = (1 - n)a_\alpha + na_\beta \quad (1)$$

where a_α and a_β are the refined lattice parameters of the α- and β-phases respectively, and n the refined fraction of the β-phase. The evolution of the cell parameter as a function of P_{H_2} at different temperatures is plotted in Figure 3b.

Similar sequences were collected through independent volumetric measurements resulting in the pressure−composition isotherms reported in Figure 3c, that give information on the stoichiometric H/Pd ratio (x) at the given P_{H_2} and temperature.

4. DISCUSSION

4.1. The PdH_x Phase Diagram for Pd/C. The pressure-structure isotherms shown in parts a and b of Figure 3 are very similar to the pressure−composition curves obtained from volumetric measurements (Figure 3c), which give information on the H/Pd ratio at a given temperature and pressure. All the

DOI: 10.1021/acs.jpcc.7b04152
J. Phys. Chem. C XXXX, XXX, XXX−XXX

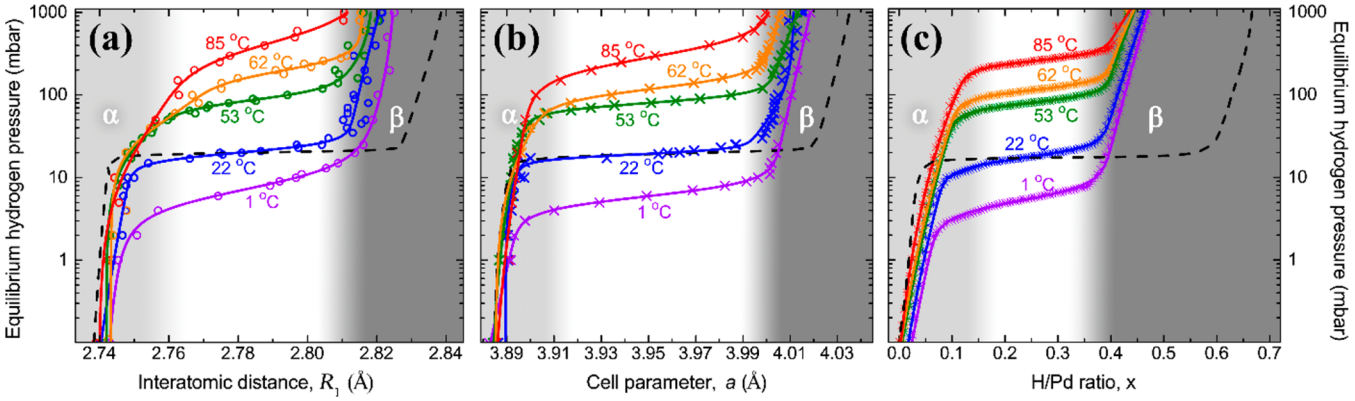

Figure 3. Pressure−R_1, pressure−a and pressure−-x isotherms obtained from EXAFS (a), XRPD (b), and volumetric techniques (c) for Pd/C at different temperatures (colored scatters) and palladium bulk (Pd-black) at 22 °C (black dashed line). Solid colored lines correspond to the best fits by a model double-exponential function. The abscissa of part (b) is the averaged cell parameter defined in eq 1. Light gray, white, and dark gray regions define qualitatively pure α-, mixed-, and pure β-phases, respectively, for the Pd/C sample.

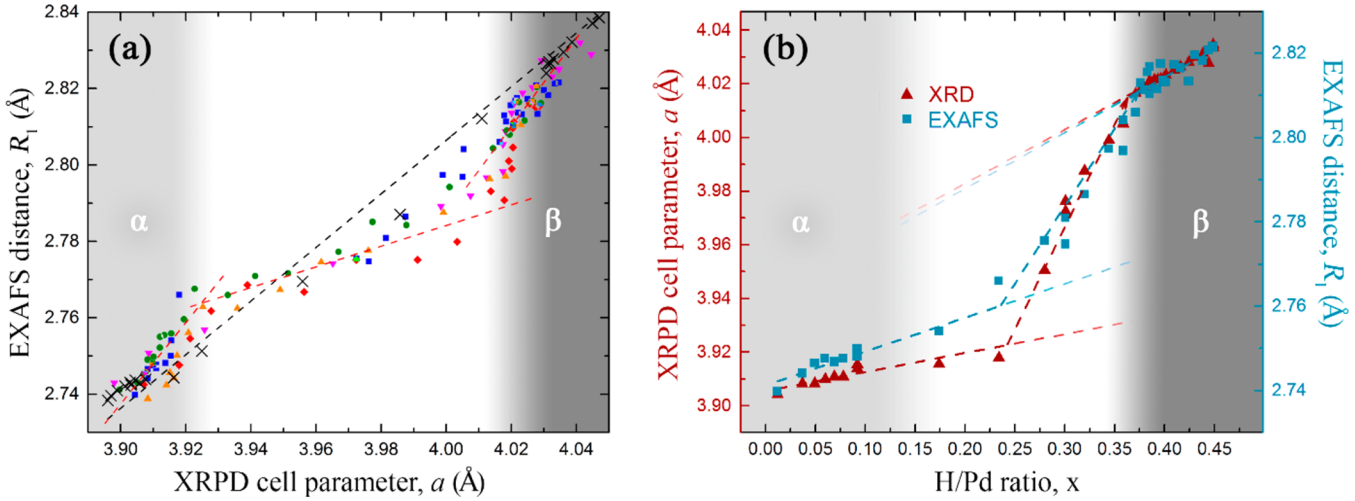

Figure 4. (a) Interatomic first shell distance R_1 obtained from EXAFS vs cell parameter a obtained from XRPD. The plot contains all the data measured at different temperatures in the pressure range from 0 to 1000 mbar. The different colors of the scatters correspond to different temperatures; the color scheme is kept the same as in Figure 3. Cross scatters refer to palladium black, and the black dashed line is a linear fit of these data. Three red dashed lines emphasize the relation between EXAFS and XRPD for the nanoparticles in the three different regions. (b) Evolution of the XRPD cell parameter (left axis, red triangles) and EXAFS interatomic distances (right axis, blue squares) with the increase of hydrogen loading in the palladium nanoparticles at 22 °C.

diagrams are characterized by three distinct regions: (i) a preplateau region, relative to the formation of the α-phase (light gray region); (ii) the plateau, corresponding to the phase transition from the solid solution to the β-phase (white region); (iii) a postplateau region, where the solid solution of hydrogen in the metal hydride is formed (dark gray region).[86] As widely reported for bulk palladium, the pressure corresponding to the plateau increases with the temperature, and at the same time the miscibility gap of the solid solution with the hydride phase decreases.[38,40,86−94]

As a consequence of the nanometric size,[36,71,86,95] for palladium nanoparticles the hydrogen-uptake and the lattice parameters at the end of each plateau is lower than that for bulk palladium at similar temperatures, e.g. at 22 °C only $PdH_{0.4}$ was obtained in Pd/C vs $PdH_{0.6}$ for palladium black. In contrast, the thermodynamics of hydrogen absorption seem not to be influenced by the nanometric size of the palladium particles. Indeed, the enthalpic and entropic values obtained from the Van 't Hoff plot reported in Figure S10 ($\Delta H = -36.9 \pm 3.7$ kJ·mol_{H2}^{-1}; $\Delta S = 92.0 \pm 9.2$ J·K^{-1}·mol_{H2}^{-1}) are close to those reported in the literature for bulk palladium ($\Delta H = -37.2$ kJ·mol_{H2}^{-1}; $\Delta S = 92.5$ J·K^{-1}·mol_{H2}^{-1}),[45] and in agreement with the values reported in the literature for nanometric palladium particles.[35,36,40,45,46,53,90,93,96−98] The absence of a clear dependence of the entropic/enthalpic terms on the palladium particle size and shape has been previously reported,[35,45,46] and explained in terms of an enthalpy−entropy compensation effect in H-absorption in both palladium bulk and nanoparticles.[45]

4.2. Evolution of the Pd−Pd Distances in the Core and Shell of the PdH_x Nanoparticles. As a general tendency, the palladium nanoparticles undergo a less sharp phase transition than bulk palladium, which was explained in the literature by size and shape dispersion phenomena.[96] This effect is evident when comparing the structural and compositional isotherms obtained at 22 °C for Pd/C (blue scatters in Figure 3) and palladium black (dashed line in Figure 3). However, the first shell EXAFS data themselves (Figure 3a) exhibit a less defined plateau than the corresponding XRPD data (Figure 3b). The plateau of the isotherms obtained by EXAFS are spanned in a

DOI: 10.1021/acs.jpcc.7b04152
J. Phys. Chem. C XXXX, XXX, XXX−XXX

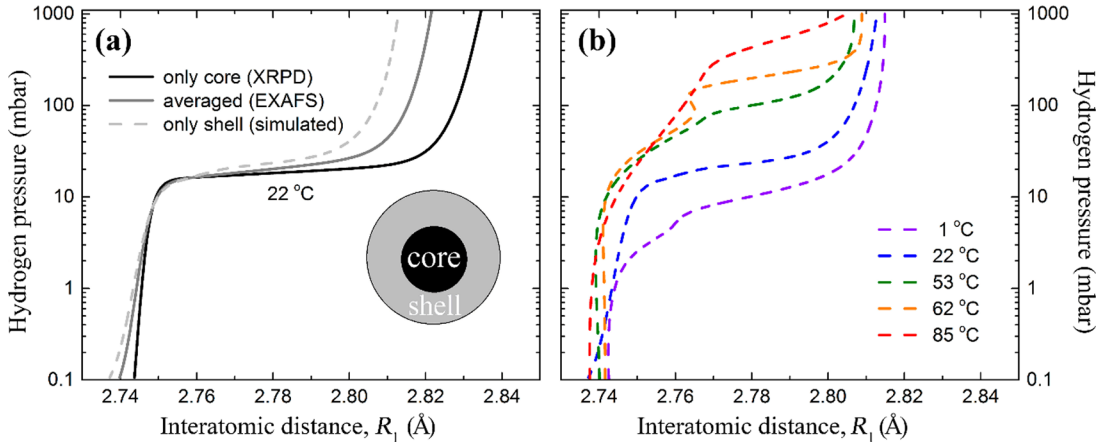

Figure 5. (a) Pressure-distance isotherms of core and shell of the palladium hydride nanoparticle plotted as a function of R_1. Full curves correspond to the experimental pressure-structure isotherms at 22 °C, as obtained from XRPD data (black) and EXAFS data (dark gray). The dashed line is the theoretical curve, obtained by applying eq 2 in the hypothesis of 60% of atoms contributing to the shell (C = 0.6, see scheme), and accounts for the behavior of palladium hydrides in the shell of the nanoparticle. (b) Simulated pressure-distance isotherms for the shell part of the nanoparticles at different temperatures. The similar simulated isotherms, assuming the shell fraction of 50 and 70% is shown in Figure S11.

wider pressure range with respect to the same plateau observed by XRPD at all the investigated temperatures. This discrepancy is absent for palladium black, suggesting that it is a characteristic feature of the sample, and not of the method.

The systematic difference in the behavior of the first shell EXAFS and XRPD data can be better appreciated by plotting the evolution of the first Pd−Pd distance obtained by EXAFS (R_1) as a function of the cell parameter a obtained by XRPD for all the different pressures and temperatures, as shown in Figure 4a. For palladium black, the data can be fitted by a straight line of the type $R_1 = m \times a$ (dashed line in Figure 4a), where the fitted value of $m = 0.71 \pm 0.01$ agrees with that expected from the geometric relationship between the cell parameter and the interatomic distance in a face centered cubic lattice, given by $1/\sqrt{2} = 0.707$. A minor difference between $\sqrt{2}\ R_1$ and a is originated from systematic error associated with each method (e.g., error in determining sample-to-detector distance in XRPD, calculated phases and correlation between E_0 and R_1 in EXAFS, etc.). To minimize this systematic error, we corrected the a values obtained for the nanoparticles by factor 0.996 determined comparing XRD and EXAFS data obtained on Pd metallic bulk. A larger deviation from this linear law is observed for palladium nanoparticles in Pd/C. In particular, in the regions corresponding to pure α- and β-phases, the first shell R_1 values obtained from EXAFS grow faster than the cell parameter obtained by XRPD, while during the phase transition an opposite behavior is observed. To emphasize this difference, in Figure 4b, the first shell R_1 and a values have been plotted as a function of the H/Pd ratio x determined from the volumetric measurements reported in Figure 3c.

The observed discrepancy can be accounted for by considering that the palladium hydride nanoparticles do have a core−shell structure, with a crystalline core that contributes both to the Bragg reflections in the XRPD patterns and to the first shell Pd−Pd distance obtained by EXAFS, and an amorphous shell that contributes only to EXAFS. Similar models of core−shell palladium hydride nanoparticles have been previously discussed, but did not have explicit experimental evidence.[40,45,46,88,99,100] It has also been shown that for nanoparticles with average size of 1 nm, which do not give well-defined Bragg peaks due to the lack of long-range order,[53,54] the α−β phase separation does not exist and the pressure−composition isotherms lack the plateau region.[52] A similar behavior should be expected for an amorphous shell of Pd hydride nanoparticle, but cannot be measured directly. Nevertheless, the theoretical R_1^{shell} (P_{H_2}) pressure-distance isotherm of the shell can be derived from the available data, by using the XRPD pressure-a isotherm, $a(P_{H_2})$, as representative of the core, and the EXAFS isotherm, R_1^{EXAFS} (P_{H_2}) as the average of the core and shell contributions, according to the following expression:

$$CR_1^{shell}(P_{H_2}) = R_1^{EXAFS}(P_{H_2}) - (1 - C)\frac{1}{\sqrt{2}}a(P_{H_2}) \quad (2)$$

where C is the fraction of atoms located in the amorphous shell. This value was set to 0.6 based on the detailed analysis of EXAFS spectra,[70] which indicated that the fraction of palladium atoms located in the amorphous surface for Pd nanoparticle of 2.6 nm size is about 60%. In addition, the crystalline size determined from XRPD (full widths of the Bragg peaks) does not change significantly along the hydride phase formation at all studied temperatures, which indicates that the ratio between core and shell can be fixed for all experimental points. The resulted theoretical isotherm (22 °C) for the amorphous shell of the nanoparticle is shown in Figure 5a together with the two experimental curves that have been used to obtain it. As expected, the shell absorbs hydrogen gradually, and the corresponding isotherm does not result in a well-defined phase transition. The similar simulated isotherms, assuming the shell fraction of 50 and 70% is shown in Figure S11.

From the data reported in Figure 5a, it emerges that the R_1 distance is shorter in the amorphous shell than in the bulk core at any investigated P_{H_2}. This difference is small at low P_{H_2} ($\Delta R_1 < 0.005$ Å) and progressively increases with the hydrogen uptake ($\Delta R_1 = 0.014$ Å). The pressure-distance isotherms obtained for the shell of the nanoparticles (Figure 5b) indicate that the shell part absolutely lack the plateau region at high temperatures. This agrees with the observation done on 1 nm Pd particles exhibiting only the amorphous phase.[52] In addition, figure emphasize the changes in the slope of the isotherms in the mixed phase region which are most strongly observed at

DOI: 10.1021/acs.jpcc.7b04152
J. Phys. Chem. C XXXX, XXX, XXX−XXX

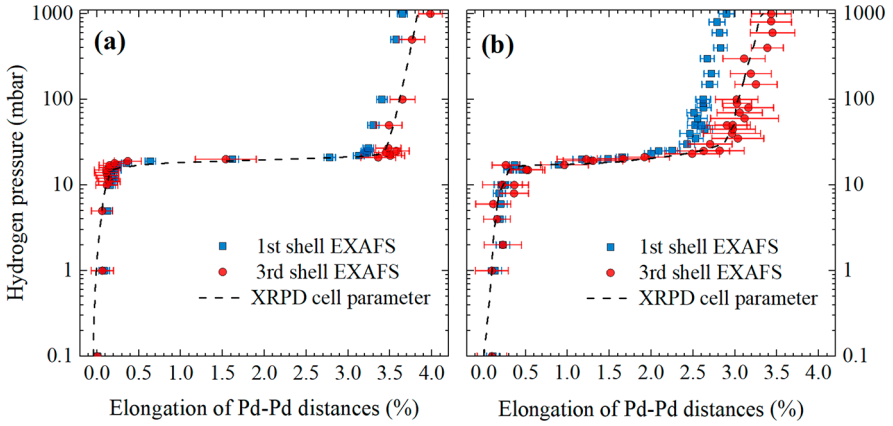

Figure 6. Evolution of the first (blue squares) and third (red circles) shells determined by EXAFS for Pd black (a) and Pd nanoparticles (b) during hydride phase formation at 22 °C. The XRPD data is shown as black dashed line.

high temperatures. The origin of such slope may be due to the fact that the critical temperature, above which no α- and β-phases do not exist, is lower in the shell than in the core. However, within the quality of the data we cannot prove or disprove this hypothesis.

As a final comment, it could be argued that, besides the amorphous shell, ultrasmall nanoparticles below 1 nm can also contribute to EXAFS, while escaping from detection by XRPD. However, in the present study, this contribution can be neglected for two reasons: (i) the fraction of particles with diameter below 2 nm is negligible (inset in Figure 1), (ii) there are less atoms inside a 1 nm particle than in the shell of a 2.6 nm particle, which further reduce their effect on the resulting EXAFS spectrum.[62,101] This means that the discrepancies observed between the EXFS and the XRPD data (Figure 4) are actually due to a core−shell effect and not to a size-heterogeneity effect.

4.3. Higher-Shell EXAFS Analysis. To further confirm the discrepancy between the results obtained from XRPD and first shell EXAFS analyses, and to support our crystalline core/amorphous shell model we report additional higher shell EXAFS analysis on the 22 °C isotherm data for Pd black (Figure 6a) and Pd nanoparticles (Figure 6b). Indeed, higher-shell analysis of EXAFS data provides intermediate-range structural information, being so intermediate between the short-range order selectivity of the first shell EXAFS analysis and the long-range order typical of XRD technique. To highlight the different behavior of first and higher shells, we have performed EXAFS-analysis in extended R-range from 1.2 to 5.5 Å, using the whole k-range available: 3.0−14.0 Å^{-1}. All contributions with an intensity higher than 0.05 (with respect to the SS first shell Pd−Pd) and with effective path length smaller than 6 Å were taken into account (see Figures S4 and S5). The decrease of coordination numbers in the nanoparticles with respect to the bulk was taken into account using an equation[79]

$$N_{nano,i} = \left[1 - \frac{3}{2}\frac{R_i}{D} + \frac{1}{2}\left(\frac{R_i}{D}\right)^3\right] N_{bulk,i} \quad (3)$$

where R_i is the effective path length of each path, and D is the mean particle size (for the bare nanoparticles, we determined D = 2.4 ± 0.8 nm which is close to the size provided by TEM and XRPD). The so obtained $N_{nanio,i}$ values were kept fixed in the fits.

Figure 6 shows the relative evolution of the interatomic distances for the first and third shells. The figure reports $\Delta R_i/R_{i,0} = (R_i - R_{i,0})/R_{i,0}$ values, with R_i being the P_{H_2}-dependent distance of the ith shell, $R_{i,0}$ the corresponding value for the pure metallic phase and i = 1 and 3. The dashed line reports the equivalent $\Delta a/a_0 = (a - a_0)/a_0$ values extracted from XRPD, with obvious meaning. It is clearly seen that for the Pd black sample the same relative elongation is observed for $\Delta R_1/R_{1,0}$, $\Delta R_3/R_{3,0}$, and $\Delta a/a_0$ (Figure 6a). Conversely, in the case of the nanoparticles (Figure 6b), the elongation of the third shell distance is bigger than that of the first shell and has a similar behavior as XRPD data. The corresponding $\Delta R_2/R_{2,0}$, $\Delta R_4/R_{4,0}$, curves, referring to the second and fourth shells are not shown in Figure 6 because their contribution to the oscillatory EXAFS function is much smaller and fully overlapped by the contribution of much stronger MS paths falling in the same R-region (see Figure S4). These facts result in bigger error in their determination.

It is worth underlying that XRPD is still fundamental in giving solidity to our core/shell model because the error associated with the determination of a by XRPD is much smaller than that related to the determination of R_3 by EXAFS.

4.4. Short and Long Scale Disorder. Both thermal and structural disorder affect both XRPD and EXAFS data, reducing the intensity of the signals at high q or k values, respectively.[102] Consequently, the disorder has been considered in the data analysis, by optimizing the isotropic atomic displacement (U_{iso}) in XRPD and the Debye−Waller parameter (σ^2) in EXAFS. For the data collected at 22 °C, the optimized U_{iso} is about 0.005 Å^2 for all the patterns in both pure metal and α- and β- hydride phases of the Pd nanoparticles (green squares in Figure 7). Indeed, U_{iso} describes the oscillation of an atom around its crystallographic position, and is almost insensitive to the crystallographic phase (note that similar U_{iso} values have been obtained for the bulk Pd black phase along the whole isotherm, gray stars). In contrast, the σ^2 obtained from EXAFS analysis is not constant, but increases with P_{H_2} (blue diamonds in Figure 7). For both nanoparticles (blue diamond) and Pd black (black crosses), the σ^2 parameter does not change in the region below 10 mbar. This fact is explained considering that the α-phase contains a very low amount of hydrogen, which does not contribute significantly to the structural disorder. An almost stepwise increase of σ^2 is then observed in the phase transition region around 20 mbar, corresponding to the coexistence of the

DOI: 10.1021/acs.jpcc.7b04152
J. Phys. Chem. C XXXX, XXX, XXX−XXX

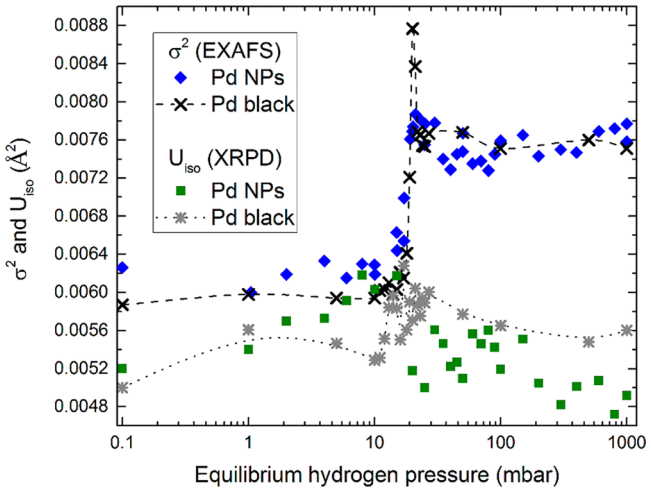

Figure 7. Evolution of the Debye–Waller parameter σ^2 (as determined by EXAFS) for the palladium nanoparticles (blue diamonds) and palladium black (black crosses highlighted by dashed line) upon the hydride phase formation at 22 °C, versus U_{iso} (as determined by XRPD analysis) for the palladium nanoparticles (green squares) and palladium black (gray starts highlighted by dotted line).

α- and β- hydride phases, that are characterized by different Pd–Pd interatomic distances. This abrupt change of σ^2 with the hydrogen uptake can be explained by considering that σ^2 reflects the variation in the interatomic distance between the neighboring atoms and includes thermal disorder and static disorder effects.[103] This effect is even more pronounced for palladium black (black crosses in Figure 7), because the difference in the Pd–Pd interatomic distances in the α- and β-hydride phases is bigger for bulk palladium than for the nanoparticles and because the phase transition occurs in a narrower P_{H_2} interval. Finally, the σ^2 in the pure β-phase does not go back to the starting value due to the significant fraction of hydrogen atoms ($x \approx 0.4$ or 0.6 for nanoparticles or bulk, respectively) incorporated in the interstitial sites of the palladium lattice. Such H atoms create local distortions of the environment of each Pd atoms (that is observed by EXAFS with an increase of σ^2), but since such distortions do not have long-range order, they are not detected with diffraction methods. A more detailed discussion on the EXAFS σ^2 parameter increase in the solid solutions can be found in the literature.[104−107]

The logical challenge that arises from the discussion reported above, would be to perform the Fourier-analysis of the EXAFS spectra using the separate contributions for the α- and β-phases, as it was done in the XRPD refinement. Indeed, such approach should decrease the values of Debye–Waller parameter in the region of the phase transition. However, in this particular case, such analysis does not give reliable results because there is a strong correlation between $|R_\beta - R_\alpha|$ and σ^2, where R_α and R_β are the first shell Pd–Pd interatomic distances within each of the phases. This correlation cannot be resolved, because it is limited by the standard resolution of the local structure distortion by EXAFS[108] due to too small value of $|R_\beta - R_\alpha|$ for the measured Δk interval (the Rietveld-refined difference $|R_\beta - R_\alpha|$ in the phase transition region is below 0.07 Å (see Figure S7 of the Supporting Information), while the spatial resolution of our EXAFS data is $\pi/(2k_{max})$[66] > 0.1 Å).

5. CONCLUSIONS

In this study, we have investigated the process of hydride formation in wide pressure and temperature ranges in carbon-supported Pd nanoparticles having an average size of (2.6 ± 0.4) nm, by coupling volumetric measurements with simultaneous EXAFS and XRPD experiments. The synergic use of the three techniques allowed constructing the PdH_x phase diagram for Pd nanoparticles. During the hydride phase formation, a systematic difference was observed in the evolution of the first shell Pd–Pd interatomic distances as determined by EXAFS and XRPD showing a difference of $\Delta R_1 = 0.014$ Å between core and shell in the β-phase. This difference was shown to be a characteristic feature of the PdH_x nanoparticles. This is the first structural direct evidence of the presence of a core/shell structure in palladium nanoparticles. The crystalline PdH_x core contributes to both XRPD and EXAFS, while the amorphous shell does not contribute to XRPD but is probed by EXAFS. The core exhibits the sharp phase transition and the flat pressure-structure plateau in the isotherms typical of bulk palladium, while the shell exhibits a much smoother behavior. The core/shell model is further supported by the analysis of the evolution of the third shell interatomic distance in the EXAFS data, that exhibits a behavior closer to that observed by XRPD rather than to that of the EXAFS first shell.

In addition, we observed for both Pd nanoparticles and bulk palladium samples a different behavior of the σ^2 parameter determined by EXAFS with respect to U_{iso} from XRPD along the hydride phase formation. This difference was explained by the fundamental difference between the long- and short-range disorder contributing to XRPD and EXAFS, respectively. Increased local disorder of the palladium hydride solid solution leads to higher σ^2 in EXAFS, while XRPD shows a similar U_{iso} parameter for both dehydrogenated material and hydride phases.

For all the results stated above, the simultaneous *in situ* EXAFS and XRPD data collection was mandatory to highlight the discrepancies between the core and the shell parts of the nanoparticles. This operando structural information is relevant for structure-sensitive reactions,[109−113] as we have been able, for the first time, to determine the actual structure of the active, amorphous catalyst surface.

■ ASSOCIATED CONTENT

Supporting Information

The Supporting Information is available free of charge on the ACS Publications website at DOI: 10.1021/acs.jpcc.7b04152.

TEM details, EXAFS analysis, XRPD data, Rietveld refinement details, Williamson–Hall analysis, and volumetric measurements details (PDF)

■ AUTHOR INFORMATION

Corresponding Authors

*(A.L.B.) E-mail: abugaev@sfedu.ru.
*(C.L.) E-mail carlo.lamberti@unito.it.

ORCID

Kirill A. Lomachenko: 0000-0003-0238-1719
Elena Groppo: 0000-0003-4153-5709
Carlo Lamberti: 0000-0001-8004-2312

Notes

The authors declare no competing financial interest.

DOI: 10.1021/acs.jpcc.7b04152
J. Phys. Chem. C XXXX, XXX, XXX−XXX

■ ACKNOWLEDGMENTS

A.L.B., A.A.G., K.A.L., V.V.S., A.V.S., and C.L. acknowledge a Mega-Grant from the Ministry of Education and Science of the Russian Federation (14.Y26.31.0001) for funding the research. A.A.G. acknowledges a grant of the President of Russia for young scientists MK-7300.2016.2. We are indebted to Vladimir Dmitriev, Herman Emerich, Wouter van Beek, and Michela Brunelli for their friendly and competent support during the experiment performed at the BM01B (now BM31) beamline of the ESRF. We also thank Michele Carosso for help in volumetric measurements. We acknowledge the stimulating and constructive comments of the reviewers who suggested to us to extend the EXAFS analysis up to the third coordination shell (section 4.3).

■ REFERENCES

(1) Beletskaya, I. P.; Cheprakov, A. V. The Heck Reaction as a Sharpening Stone of Palladium Catalysis. *Chem. Rev.* **2000**, *100*, 3009−3066.

(2) Lu, Z. H.; Liu, G. J.; Phillips, H.; Hill, J. M.; Chang, J.; Kydd, R. A. Palladium Nanoparticle Catalyst Prepared in Poly(Acrylic Acid)-Lined Channels of Diblock Copolymer Microspheres. *Nano Lett.* **2001**, *1*, 683−687.

(3) Gopidas, K. R.; Whitesell, J. K.; Fox, M. A. Synthesis, Characterization, and Catalytic Applications of a Palladium-Nanoparticle-Cored Dendrimer. *Nano Lett.* **2003**, *3*, 1757−1760.

(4) Barbaro, P.; Bianchini, C.; Dal Santo, V.; Meli, A.; Moneti, S.; Psaro, R.; Scaffidi, A.; Sordelli, L.; Vizza, F. Hydrogenation of Arenes Over Silica-Supported Catalysts that Combine a Grafted Rhodium Complex and Palladium Nanoparticles: Evidence for Substrate Activation on Rh Single-Site-Pd-Metal Moieties. *J. Am. Chem. Soc.* **2006**, *128*, 7065−7076.

(5) Phan, N. T. S.; Van Der Sluys, M.; Jones, C. W. on The Nature of The Active Species in Palladium Catalyzed Mizoroki-Heck and Suzuki-Miyaura Couplings - Homogeneous or Heterogeneous Catalysis, a Critical Review. *Adv. Synth. Catal.* **2006**, *348*, 609−679.

(6) Kantchev, E. A. B.; O'Brien, C. J.; Organ, M. G. Palladium Complexes of N-Heterocyclic Carbenes as Catalysts for Cross-Coupling Reactions - a Synthetic Chemist's Perspective. *Angew. Chem., Int. Ed.* **2007**, *46*, 2768−2813.

(7) Yin, L. X.; Liebscher, J. Carbon-Carbon Coupling Reactions Catalyzed by Heterogeneous Palladium Catalysts. *Chem. Rev.* **2007**, *107*, 133−173.

(8) Park, J. N.; forman, A. J.; Tang, W.; Cheng, J. H.; Hu, Y. S.; Lin, H. F.; Mcfarland, E. W. Highly Active and Sinter-Resistant Pd-Nanoparticle Catalysts Encapsulated in Silica. *Small* **2008**, *4*, 1694−1697.

(9) Li, Y.; Fan, X. B.; Qi, J. J.; Ji, J. Y.; Wang, S. L.; Zhang, G. L.; Zhang, F. B. Palladium Nanoparticle-Graphene Hybrids as Active Catalysts for the Suzuki Reaction. *Nano Res.* **2010**, *3*, 429−437.

(10) Xu, X.; Li, Y.; Gong, Y. T.; Zhang, P. F.; Li, H. R.; Wang, Y. Synthesis of Palladium Nanoparticles Supported on Mesoporous N-Doped Carbon and their Catalytic Ability for Biofuel Upgrade. *J. Am. Chem. Soc.* **2012**, *134*, 16987−16990.

(11) Pun, D.; Diao, T. N.; Stahl, S. S. Aerobic Dehydrogenation of Cyclohexanone to Phenol Catalyzed by $Pd(TFA)_2$/2-Dimethylamino-pyridine: Evidence for the Role of Pd Nanoparticles. *J. Am. Chem. Soc.* **2013**, *135*, 8213−8221.

(12) Lei, Y.; Lu, J.; Luo, X. Y.; Wu, T. P.; Du, P.; Zhang, X. Y.; Ren, Y.; Wen, J. G.; Miller, D. J.; et al. Synthesis of Porous Carbon Supported Palladium Nanoparticle Catalysts by Atomic Layer Deposition: Application for Rechargeable Lithium-O_2 Battery. *Nano Lett.* **2013**, *13*, 4182−4189.

(13) Jie, X. M.; Shang, Y. P.; Hu, P.; Su, W. P. Palladium-Catalyzed Oxidative Cross-Coupling between Heterocycles and Terminal Alkynes with low Catalyst Loading. *Angew. Chem., Int. Ed.* **2013**, *52*, 3630−3633.

(14) Chinchilla, R.; Najera, C. Chemicals from Alkynes with Palladium Catalysts. *Chem. Rev.* **2014**, *114*, 1783−1826.

(15) Deraedt, C.; Astruc, D. "Homeopathic" Palladium Nanoparticle Catalysis of Cross Carbon-Carbon Coupling Reactions. *Acc. Chem. Res.* **2014**, *47*, 494−503.

(16) Zhu, Q. L.; Tsumori, N.; Xu, Q. Immobilizing Extremely Catalytically Active Palladium Nanoparticles to Carbon Nanospheres: a Weakly-Capping Growth Approach. *J. Am. Chem. Soc.* **2015**, *137*, 11743−11748.

(17) Mondal, B.; Acharyya, K.; Howlader, P.; Mukherjee, P. S. Molecular Cage Impregnated Palladium Nanoparticles: Efficient, Additive-Free Heterogeneous Catalysts for Cyanation of Aryl Halides. *J. Am. Chem. Soc.* **2016**, *138*, 1709−1716.

(18) Rahimi, F.; Iraji zad, A. I. Characterization of Pd Nanoparticle Dispersed over Porous Silicon as a Hydrogen Sensor. *J. Phys. D: Appl. Phys.* **2007**, *40*, 7201−7209.

(19) Sugawa, K.; Tahara, H.; Yamashita, A.; Otsuki, J.; Sagara, T.; Harumoto, T.; Yanagida, S. Refractive Index Susceptibility of the Plasmonic Palladium Nanoparticle: Potential as the third Plasmonic Sensing Material. *ACS Nano* **2015**, *9*, 1895−1904.

(20) Huang, J. S.; Liu, Y.; Hou, H. Q.; You, T. Y. Simultaneous Electrochemical Determination of Dopamine, Uric Acid and Ascorbic Acid Using Palladium Nanoparticle-Loaded Carbon Nanofibers Modified Electrode. *Biosens. Bioelectron.* **2008**, *24*, 632−637.

(21) Huang, J. S.; Wang, D. W.; Hou, H. Q.; You, T. Y. Electrospun Palladium Nanoparticle-Loaded Carbon Nanofibers and their Electrocatalytic Activities towards Hydrogen Peroxide and NADH. *Adv. Funct. Mater.* **2008**, *18*, 441−448.

(22) Lu, L. M.; Li, H. B.; Qu, F. L.; Zhang, X. B.; Shen, G. L.; Yu, R. Q. in Situ Synthesis of Palladium Nanoparticle-Graphene Nanohybrids and their Application in Nonenzymatic Glucose Biosensors. *Biosens. Bioelectron.* **2011**, *26*, 3500−3504.

(23) Zeng, Q.; Cheng, J. S.; Liu, X. F.; Bai, H. T.; Jiang, J. H. Palladium Nanoparticle/Chitosan-Grafted Graphene Nanocomposites for Construction of a Glucose Biosensor. *Biosens. Bioelectron.* **2011**, *26*, 3456−3463.

(24) Wang, H.; Zhang, Y.; Li, H.; Du, B.; Ma, H. M.; Wu, D.; Wei, Q. A Silver-Palladium Alloy Nanoparticle-Based Electrochemical Biosensor for Simultaneous Detection of Ractopamine, Clenbuterol and Salbutamol. *Biosens. Bioelectron.* **2013**, *49*, 14−19.

(25) Gao, D. F.; Zhou, H.; Wang, J.; Miao, S.; Yang, F.; Wang, G. X.; Wang, J. G.; Bao, X. H. Size-Dependent Electrocatalytic Reduction of CO_2 over Pd Nanoparticles. *J. Am. Chem. Soc.* **2015**, *137*, 4288−4291.

(26) Armbrüster, M.; Behrens, M.; Cinquini, F.; Föttinger, K.; Grin, Y.; Haghofer, A.; Klötzer, B.; Knop-Gericke, A.; Lorenz, H.; et al. How to Control the Selectivity of Palladium-Based Catalysts in Hydrogenation Reactions: the Role of Subsurface Chemistry. *ChemCatChem* **2012**, *4*, 1048−1063.

(27) Borodziński, A.; Bond, G. C. Selective Hydrogenation of Ethyne in Ethene-Rich Streams on Palladium Catalysts, Part 2: Steady-State Kinetics and Effects of Palladium Particle Size, Carbon Monoxide, and Promoters. *Catal. Rev.: Sci. Eng.* **2008**, *50*, 379−469.

(28) Borodziński, A.; Bond, G. C. Selective Hydrogenation of Ethyne in Ethene-Rich Streams on Palladium Catalysts. Part 1. Effect of Changes to the Catalyst During Reaction. *Catal. Rev.: Sci. Eng.* **2006**, *48*, 91−144.

(29) Borodziński, A. The Effect of Palladium Particle Size on the Kinetics of Hydrogenation of Acetylene−Ethylene Mixtures Over Pd/SiO_2 Catalysts. *Catal. Lett.* **2001**, *71*, 169−175.

(30) Molnar, A.; Sarkany, A.; Varga, M. Hydrogenation of Carbon-Carbon Multiple Bonds: Chemo-, Regio- and Stereo-Selectivity. *J. Mol. Catal. A: Chem.* **2001**, *173*, 185−221.

(31) Tew, M. W.; Nachtegaal, M.; Janousch, M.; Huthwelker, T.; Van Bokhoven, J. A. The Irreversible formation of Palladium Carbide During Hydrogenation of 1-Pentyne Over Silica-Supported Palladium Nanoparticles: in Situ Pd K and L_3 Edge XAS. *Phys. Chem. Chem. Phys.* **2012**, *14*, 5761−5768.

DOI: 10.1021/acs.jpcc.7b04152
J. Phys. Chem. C XXXX, XXX, XXX−XXX

(32) Tew, M. W.; Janousch, M.; Huthwelker, T.; Van Bokhoven, J. A. The Roles of Carbide and Hydride in Oxide-Supported Palladium Nanoparticles for Alkyne Hydrogenation. *J. Catal.* **2011**, *283*, 45−54.
(33) Moreno-Manas, M.; Pleixats, R. formation of Carbon-Carbon Bonds Under Catalysis by Transition-Metal Nanoparticles. *Acc. Chem. Res.* **2003**, *36*, 638−643.
(34) Pellegrini, R.; Agostini, G.; Groppo, E.; Piovano, A.; Leofanti, G.; Lamberti, C. 0.5 Wt.% Pd/C Catalyst for Purification of Terephthalic Acid: Irreversible Deactivation in Industrial Plants. *J. Catal.* **2011**, *280*, 150−160.
(35) Berube, V.; Radtke, G.; Dresselhaus, M.; Chen, G. Size Effects on the Hydrogen Storage Properties of Nanostructured Metal Hydrides: a Review. *Int. J. Energy Res.* **2007**, *31*, 637−663.
(36) Griessen, R.; Strohfeldt, N.; Giessen, H. thermodynamics of the Hybrid Interaction of Hydrogen with Palladium Nanoparticles. *Nat. Mater.* **2016**, *15*, 311−317.
(37) Jobic, H.; Renouprez, A. formation of Hydrides in Small Particles of Palladium Supported in Y-Zeolite. *J. Less-Common Met.* **1987**, *129*, 311−316.
(38) Johansson, M.; Skulason, E.; Nielsen, G.; Murphy, S.; Nielsen, R. M.; Chorkendorff, I. Hydrogen Adsorption on Palladium and Palladium Hydride at 1 bar. *Surf. Sci.* **2010**, *604*, 718−729.
(39) Kishore, S.; Nelson, J. A.; Adair, J. H.; Eklund, P. C. Hydrogen Storage in Spherical and Platelet Palladium Nanoparticles. *J. Alloys Compd.* **2005**, *389*, 234−242.
(40) Langhammer, C.; Zhdanov, V. P.; Zoric, I.; Kasemo, B. Size-Dependent Hysteresis in the formation and Decomposition of Hydride in Metal Nanoparticles. *Chem. Phys. Lett.* **2010**, *488*, 62−66.
(41) Mccaulley, J. A. in-Situ X-Ray Absorption Spectroscopy Studies of Hydride and Carbide formation in Supported Palladium Catalysts. *J. Phys. Chem.* **1993**, *97*, 10372−10379.
(42) Nag, N. K. a Study on the formation of Palladium Hydride in a Carbon-Supported Palladium Catalyst. *J. Phys. Chem. B* **2001**, *105*, 5945−5949.
(43) Shegai, T.; Langhammer, C. Hydride formation in Single Palladium and Magnesium Nanoparticles Studied by Nanoplasmonic Dark-Field Scattering Spectroscopy. *Adv. Mater.* **2011**, *23*, 4409−4414.
(44) Soldatov, A.; Della Longa, S.; Bianconi, A. Relevant Role of Hydrogen atoms in the XANES of Pd Hydride: Evidence of Hydrogen Induced Unoccupied States. *Solid State Commun.* **1993**, *85*, 863−868.
(45) Syrenova, S.; Wadell, C.; Nugroho, F. A. A.; Gschneidtner, T. A.; Diaz Fernandez, Y. A. D.; Nalin, G.; Switlik, D.; Westerlund, F.; Antosiewicz, T. J.; et al. Hydride formation thermodynamics and Hysteresis in Individual Pd Nanocrystals with Different Size and Shape. *Nat. Mater.* **2015**, *14*, 1236−1244.
(46) Wadell, C.; Pingel, T.; Olsson, E.; Zoric, I.; Zhdanov, V. P.; Langhammer, C. thermodynamics of Hydride formation and Decomposition in Supported sub-10 nm Pd Nanoparticles of Different Sizes. *Chem. Phys. Lett.* **2014**, *603*, 75−81.
(47) Bauer, M.; Schoch, R.; Shao, L.; Zhang, B.; Knop-Gericke, A.; Willinger, M.; Schlögl, R.; Teschner, D. Structure−Activity Studies on Highly Active Palladium Hydrogenation Catalysts by X-Ray Absorption Spectroscopy. *J. Phys. Chem. C* **2012**, *116*, 22375−22385.
(48) Bugaev, A. L.; Guda, A. A.; Lazzarini, A.; Lomachenko, K. A.; Groppo, E.; Pellegrini, R.; Piovano, A.; Emerich, H.; Soldatov, A. V.; et al. In Situ formation of Hydrides and Carbides in Palladium Catalyst: When XANES is Better than EXAFS and XRD. *Catal. Today* **2017**, *283*, 119−126.
(49) Teschner, D.; Borsodi, J.; Wootsch, A.; Revay, Z.; Havecker, M.; Knop-Gericke, A.; Jackson, S. D.; Schlögl, R. The Roles of Subsurface Carbon and Hydrogen in Palladium-Catalyzed Alkyne Hydrogenation. *Science* **2008**, *320*, 86−89.
(50) Teschner, D.; Borsodi, J.; Kis, Z.; Szentmiklósi, L.; Révay, Z.; Knop-Gericke, A.; Schlögl, R.; Torres, D.; Sautet, P. Role of Hydrogen Species in Palladium-Catalyzed Alkyne Hydrogenation. *J. Phys. Chem. C* **2010**, *114*, 2293−2299.
(51) Lewis, F. A. The Palladium-Hydrogen System. *Platin. Met. Rev.* **1982**, *26*, 70−78.
(52) Langhammer, C.; Larsson, E. M.; Kasemo, B.; Zoric, I. Indirect Nanoplasmonic Sensing: Ultrasensitive Experimental Platform for Nanomaterials Science and Optical Nanocalorimetry. *Nano Lett.* **2010**, *10*, 3529−3538.
(53) Ingham, B.; toney, M. F.; Hendy, S. C.; Cox, T.; Fong, D. D.; Eastman, J. A.; Fuoss, P. H.; Stevens, K. J.; Lassesson, A. Particle Size Effect of Hydrogen-Induced Lattice Expansion of Palladium Nanoclusters. *Phys. Rev. B: Condens. Matter Mater. Phys.* **2008**, *78*, 245408.
(54) Narehood, D.; Kishore, S.; Goto, H.; Adair, J.; Nelson, J.; Gutierrez, H.; Eklund, P. X-Ray Diffraction and H-Storage in Ultra-Small Palladium Particles. *Int. J. Hydrogen Energy* **2009**, *34*, 952−960.
(55) Rehr, J. J.; Albers, R. C. Theoretical Approaches to X-Ray Absorption Fine Structure. *Rev. Mod. Phys.* **2000**, *72*, 621−654.
(56) Chiarello, G. L.; Ferri, D. Modulated Excitation Extended X-Ray Absorption Fine Structure Spectroscopy. *Phys. Chem. Chem. Phys.* **2015**, *17*, 10579−10591.
(57) Ferri, D.; Kumar, M. S.; Wirz, R.; Eyssler, A.; Korsak, O.; Hug, P.; Weidenkaff, A.; Newton, M. A. First Steps in Combining Modulation Excitation Spectroscopy with Synchronous Dispersive EXAFS/DRIFTS/Mass Spectrometry for in Situ Time Resolved Study of Heterogeneous Catalysts. *Phys. Chem. Chem. Phys.* **2010**, *12*, 5634−5646.
(58) Ferri, D.; Newton, M. A.; Di Michiel, M.; Chiarello, G. L.; Yoon, S.; Lu, Y.; Andrieux, J. Revealing the Dynamic Structure of Complex Solid Catalysts Using Modulated Excitation X-Ray Diffraction. *Angew. Chem., Int. Ed.* **2014**, *53*, 8890−8894.
(59) Frenkel, A. I.; Hills, C. W.; Nuzzo, R. G. a View From the Inside: Complexity in the atomic Scale Ordering of Supported Metal Nanoparticles. *J. Phys. Chem. B* **2001**, *105*, 12689−12703.
(60) Frenkel, A. I.; Yevick, A.; Cooper, C.; Vasic, R. Modeling the Structure and Composition of Nanoparticles by Extended X-Ray Absorption Fine-Structure Spectroscopy. *Annu. Rev. Anal. Chem.* **2011**, *4*, 23−39.
(61) Frenkel, A. I. Applications of Extended X-Ray Absorption Fine-Structure Spectroscopy to Studies of Bimetallic Nanoparticle Catalysts. *Chem. Soc. Rev.* **2012**, *41*, 8163−8178.
(62) Agostini, G.; Pellegrini, R.; Leofanti, G.; Bertinetti, L.; Bertarione, S.; Groppo, E.; Zecchina, A.; Lamberti, C. Determination of the Particle Size, Available Surface Area, and Nature of Exposed Sites for Silica-Alumina-Supported Pd Nanoparticles: a Multitechnical Approach. *J. Phys. Chem. C* **2009**, *113*, 10485−10492.
(63) Agostini, G.; Piovano, A.; Bertinetti, L.; Pellegrini, R.; Leofanti, G.; Groppo, E.; Lamberti, C. Effect of Different Face Centered Cubic Nanoparticle Distributions on Particle Size and Surface Area Determination: a Theoretical Study. *J. Phys. Chem. C* **2014**, *118*, 4085−4094.
(64) Van Bokhoven, J. A.; Lamberti, C. *X-Ray Absorption and X-Ray Emission Spectroscopy: Theory and Applications*. Wiley & Sons: Chichester, U.K., 2016.
(65) Mino, L.; Agostini, G.; Borfecchia, E.; Gianolio, D.; Piovano, A.; Gallo, E.; Lamberti, C. Low-Dimensional Systems Investigated by X-Ray Absorption Spectroscopy: a Selection of 2D, 1D and 0D Cases. *J. Phys. D: Appl. Phys.* **2013**, *46*, 423001.
(66) Bordiga, S.; Groppo, E.; Agostini, G.; Van Bokhoven, J. A.; Lamberti, C. Reactivity of Surface Species in Heterogeneous Catalysts Probed by in Situ X-Ray Absorption Techniques. *Chem. Rev.* **2013**, *113*, 1736−1850.
(67) Manzoli, M.; Vindigni, F.; Tabakova, T.; Lamberti, C.; Dimitrov, D.; Ivanov, K.; Agostini, G. Structure-Reactivity Relationship in Co_3O_4 Promoted Au/Ceo_2 Catalysts for the CH_3OH Oxidation Reaction Revealed by in Situ FTIR and Operando EXAFS Studies. *J. Mater. Chem. A* **2017**, *5*, 2083−2094.
(68) Bugaev, A. L.; Guda, A. A.; Lomachenko, K. A.; Lazzarini, A.; Srabionyan, V. V.; Vitillo, J. G.; Piovano, A.; Groppo, E.; Bugaev, L. A. Hydride Phase formation in Carbon Supported Palladium Hydride Nanoparticles by in Situ EXAFS and XRD. *J. Phys.: Conf. Ser.* **2016**, *712*, 012032.
(69) Campesi, R.; Cuevas, F.; Gadiou, R.; Leroy, E.; Hirscher, M.; Vix-Guterl, C.; Latroche, M. Hydrogen Storage Properties of Pd

DOI: 10.1021/acs.jpcc.7b04152
J. Phys. Chem. C XXXX, XXX, XXX−XXX

Nanoparticle/Carbon Template Composites. *Carbon* **2008**, *46*, 206−214.
(70) Srabionyan, V. V.; Bugaev, A. L.; Pryadchenko, V. V.; Avakyan, L. A.; Van Bokhoven, J. A.; Bugaev, L. A. EXAFS Study of Size Dependence of atomic Structure in Palladium Nanoparticles. *J. Phys. Chem. Solids* **2014**, *75*, 470−476.
(71) Zlotea, C.; Cuevas, F.; Paul-Boncour, V.; Leroy, E.; Dibandjo, P.; Gadiou, R.; Vix-Guterl, C.; Latroche, M. Size-Dependent Hydrogen Sorption in Ultrasmall Pd Clusters Embedded in a Mesoporous Carbon Template. *J. Am. Chem. Soc.* **2010**, *132*, 7720−7729.
(72) Poncelet, G.; Jacobs, P.; Grange, P. *Preparation of Catalysts III*. Elsevier: 1983; Vol. *16*.
(73) Piovano, A.; Lazzarini, A.; Pellegrini, R.; Leofanti, G.; Agostini, G.; Rudić, S.; Bugaev, A. L.; Lamberti, C.; Groppo, E. Progress in the Characterization of the Surface Species in Activated Carbons by Means of INS Spectroscopy Coupled with Detailed DFT Calculations. *Adv. Condens. Matter Phys.* **2015**, *2015*, 1−8.
(74) Agostini, G.; Lamberti, C.; Pellegrini, R.; Leofanti, G.; Giannici, F.; Longo, A.; Groppo, E. Effect of Pre-Reduction on the Properties and the Catalytic Activity of Pd/Carbon Catalysts: a Comparison with Pd/Al_2O_3. *ACS Catal.* **2014**, *4*, 187−194.
(75) Van Beek, W.; Safonova, O. V.; Wiker, G.; Emerich, H. SNBL, a Dedicated Beamline for Combinedin Situ X-Ray Diffraction, X-Ray Absorption and Raman Scattering Experiments. *Phase Transitions* **2011**, *84*, 726−732.
(76) Abdala, P. M.; Safonova, O. V.; Wiker, G.; Van Beek, W.; Emerich, H.; Van Bokhoven, J. A.; Sa, J.; Szlachetko, J.; Nachtegaal, M. Scientific Opportunities for Heterogeneous Catalysis Research at the Superxas and SNBL Beam Lines. *Chimia* **2012**, *66*, 699−705.
(77) Groppo, E.; Agostini, G.; Piovano, A.; Muddada, N. B.; Leofanti, G.; Pellegrini, R.; Portale, G.; Longo, A.; Lamberti, C. Effect of Reduction in Liquid Phase on the Properties and the Catalytic Activity of Pd/Al_2O_3 Catalysts. *J. Catal.* **2012**, *287*, 44−54.
(78) Ravel, B.; Newville, M. ATHENA, ARTEMIS, HEPHAESTUS: Data Analysis for X-Ray Absorption Spectroscopy Using IFEFFIT. *J. Synchrotron Radiat.* **2005**, *12*, 537−541.
(79) Calvin, S.; Miller, M. M.; Goswami, R.; Cheng, S. F.; Mulvaney, S. P.; Whitman, L. J.; Harris, V. G. Determination of Crystallite Size in a Magnetic Nanocomposite Using Extended X-Ray Absorption Fine Structure. *J. Appl. Phys.* **2003**, *94*, 778−783.
(80) Groppo, E.; Prestipino, C.; Lamberti, C.; Luches, P.; Giovanardi, C.; Boscherini, F. Growth of NiO on Ag(001): atomic Environment, Strain, and Interface Relaxations Studied by Polarization Dependent Extended X-Ray Absorption Fine Structure. *J. Phys. Chem. B* **2003**, *107*, 4597−4606.
(81) Borfecchia, E.; Maurelli, S.; Gianolio, D.; Groppo, E.; Chiesa, M.; Bonino, F.; Lamberti, C. Insights into Adsorption of NH_3 on HKUST-1 Metal-Organic Framework: a Multitechnique Approach. *J. Phys. Chem. C* **2012**, *116*, 19839−19850.
(82) Borfecchia, E.; Lomachenko, K. A.; Giordanino, F.; Falsig, H.; Beato, P.; Soldatov, A. V.; Bordiga, S.; Lamberti, C. Revisiting the Nature of Cu Sites in the Activated Cu-SSZ-13 Catalyst for SCR Reaction. *Chem. Sci.* **2015**, *6*, 548−563.
(83) Zabinsky, S. I.; Rehr, J. J.; Ankudinov, A.; Albers, R. C.; Eller, M. J. Multiple-Scattering Calculations of X-Ray-Absorption Spectra. *Phys. Rev. B: Condens. Matter Mater. Phys.* **1995**, *52*, 2995−3009.
(84) Kieffer, J.; Wright, J. P. Pyfai: a Python Library for High Performance Azimuthal Integration on GPU. *Powder Diffr.* **2013**, *28*, S339−S350.
(85) Petříček, V.; Dušek, M.; Palatinus, L. Crystallographic Computing System JANA2006: General Features. *Z. Kristallogr. - Cryst. Mater.* **2014**, *229*, 345−352.
(86) Zuttel, A.; Nutzenadel, C.; Schmid, G.; Emmenegger, C.; Sudan, P.; Schlapbach, L. thermodynamic Aspects of the Interaction of Hydrogen with Pd Clusters. *Appl. Surf. Sci.* **2000**, *162-163*, 571−575.
(87) Eastman, J. A.; Thompson, L. J.; Kestel, B. J. Narrowing of the Palladium-Hydrogen Miscibility Gap in Nanocrystalline Palladium. *Phys. Rev. B: Condens. Matter Mater. Phys.* **1993**, *48*, 84−92.
(88) Langhammer, C.; Zhdanov, V. P.; Zorić, I.; Kasemo, B. Size-Dependent Kinetics of Hydriding and Dehydriding of Pd Nanoparticles. *Phys. Rev. Lett.* **2010**, *104*, 135502.
(89) Pundt, A.; Suleiman, M.; Bahtz, C.; Reetz, M. T.; Kirchheim, R.; Jisrawi, N. M. Hydrogen and Pd-Clusters. *Mater. Sci. Eng., B* **2004**, *108*, 19−23.
(90) Sachs, C.; Pundt, A.; Kirchheim, R.; Winter, M.; Reetz, M. T.; Fritsch, D. Solubility of Hydrogen in Single-Sized Palladium Clusters. *Phys. Rev. B: Condens. Matter Mater. Phys.* **2001**, *64*, 075408.
(91) Suleiman, M.; Faupel, J.; Borchers, C.; Krebs, H. U.; Kirchheim, R.; Pundt, A. Hydrogen Absorption Behaviour in Nanometer Sized Palladium Samples Stabilised in Soft and Hard Matrix. *J. Alloys Compd.* **2005**, *404-406*, 523−528.
(92) Suleiman, M.; Jisrawi, N. M.; Dankert, O.; Reetz, M. T.; Bahtz, C.; Kirchheim, R.; Pundt, A. Phase Transition and Lattice Expansion During Hydrogen Loading of Nanometer Sized Palladium Clusters. *J. Alloys Compd.* **2003**, *356-357*, 644−648.
(93) Yamauchi, M.; Ikeda, R.; Kitagawa, H.; Takata, M. Nanosize Effects on Hydrogen Storage in Palladium. *J. Phys. Chem. C* **2008**, *112*, 3294−3299.
(94) Yamauchi, M.; Kitagawa, H. Hydrogen Absorption of the Polymer-Coated Pd Nanoparticle. *Synth. Met.* **2005**, *153*, 353−356.
(95) Flanagan, T. B.; Oates, W. A. the Palladium-Hydrogen System. *Annu. Rev. Mater. Sci.* **1991**, *21*, 269−304.
(96) Baldi, A.; Narayan, T. C.; Koh, A. L.; Dionne, J. A. In Situ Detection of Hydrogen-Induced Phase Transitions in Individual Palladium Nanocrystals. *Nat. Mater.* **2014**, *13*, 1143−1148.
(97) Bardhan, R.; Hedges, L. O.; Pint, C. L.; Javey, A.; Whitelam, S.; Urban, J. J. Uncovering the Intrinsic Size Dependence of Hydriding Phase Transformations in Nanocrystals. *Nat. Mater.* **2013**, *12*, 905−912.
(98) Fischer, F. D.; Waitz, T.; Vollath, D.; Simha, N. K. On the Role of Surface Energy and Surface Stress in Phase-Transforming Nanoparticles. *Prog. Mater. Sci.* **2008**, *53*, 481−527.
(99) Ren, H.; Zhang, T.-Y. H Concentrations and Stresses in Pd Nanoparticles. *Mater. Lett.* **2014**, *130*, 176−179.
(100) Zhdanov, V. P.; Kasemo, B. Kinetics of the formation of a New Phase in Nanoparticles. *Chem. Phys. Lett.* **2008**, *460*, 158−161.
(101) Braglia, L.; Borfecchia, E.; Lomachenko, K. A.; Bugaev, A. L.; Guda, A. A.; Soldatov, A. V.; Bleken, B. T. L.; Oien-Odegaard, S.; Olsbye, U.; et al. Tuning Pt and Cu Sites Population Inside Functionalized UiO-67 MOF by Controlling Activation Conditions. *Faraday Discuss.* **2017**, DOI: 10.1039/C7FD00024C.
(102) Borfecchia, E.; Gianolio, D.; Agostini, G.; Bordiga, S.; Lamberti, C. Characterization of MOFs. 2. Long and Local Range Order Structural Determination of MOFs by Combining EXAFS and Diffraction Techniques. In *Metal Organic Frameworks as Heterogeneous Catalysts*, Llabrés, I.; Xamena, F.; Gascón, J., Eds.; The Royal Society of Chemistry: Cambridge, U.K., 2013; pp 143−208.
(103) fornasini, P.; Grisenti, R. on EXAFS Debye-Waller Factor and Recent Advances. *J. Synchrotron Radiat.* **2015**, *22*, 1242−1257.
(104) Lebedev, A. I.; Sluchinskaya, I. A.; Demin, V. N.; Munro, I. EXAFS Studies of the Local Environment of Lead and Selenium atoms in $PbTe_{1-x}Se_x$ Solid Solutions. *Phys. Solid State* **1999**, *41*, 1275−1282.
(105) Razmara, M. F.; Henderson, C. M. B.; Pattrick, R. A. D.; Bell, A. M. T.; Charnock, J. M. the Crystal Chemistry of the Solid Solution Series Between Chalcostibite ($CuSbS_2$) and Emplectite ($CuBiS_2$). *Mineral. Mag.* **1997**, *61*, 79−88.
(106) Kuzmin, A.; Mironova, N.; Purans, J.; Sazonov, A. EXAFS and XANES Studies of $Co_xMg_{1-x}O$ Solid Solutions Using a Laboratory EXAFS Spectrometer. *Phys. Status Solidi a* **1993**, *135*, 133−141.
(107) Romanato, F.; De Salvador, D.; Berti, M.; Drigo, A.; Natali, M.; tormen, M.; Rossetto, G.; Pascarelli, S.; Boscherini, F.; et al. Bond-Length Variation in $In_xGa_{1-x}As/InP$ Strained Epitaxial Layers. *Phys. Rev. B: Condens. Matter Mater. Phys.* **1998**, *57*, 14619−14622.
(108) Bugaev, L. A.; Avakyan, L. A.; Srabionyan, V. V.; Bugaev, A. L. Resolution of Interatomic Distances in the Study of Local atomic Structure Distortions by Energy-Restricted X-Ray Absorption Spectra. *Phys. Rev. B: Condens. Matter Mater. Phys.* **2010**, *82*, 064204.

DOI: 10.1021/acs.jpcc.7b04152
J. Phys. Chem. C XXXX, XXX, XXX−XXX

(109) Lv, C. Q.; Ling, K. C.; Wang, G. C. Methane Combustion on Pd-Based Model Catalysts: Structure Sensitive or Insensitive? *J. Chem. Phys.* **2009**, *131*, 144704.
(110) Van Santen, R. A. Complementary Structure Sensitive and Insensitive Catalytic Relationships. *Acc. Chem. Res.* **2009**, *42*, 57−66.
(111) Sanchez-Sanchez, C. M.; Solla-Gullon, J.; Vidal-Iglesias, F. J.; Aldaz, A.; Montiel, V.; Herrero, E. Imaging Structure Sensitive Catalysis on Different Shape-Controlled Platinum Nanoparticles. *J. Am. Chem. Soc.* **2010**, *132*, 5622−5624.
(112) Childers, D. J.; Schweitzer, N. M.; Shahari, S. M. K.; Rioux, R. M.; Miller, J. T.; Meyer, R. J. Modifying Structure-Sensitive Reactions by Addition of Zn to Pd. *J. Catal.* **2014**, *318*, 75−84.
(113) Li, Y. F.; Cui, F.; Ross, M. B.; Kim, D.; Sun, Y.; Yang, P. D. Structure-Sensitive CO_2 Electroreduction to Hydrocarbons on Ultrathin 5-Fold Twinned Copper Nanowires. *Nano Lett.* **2017**, *17*, 1312−1317.

DOI: 10.1021/acs.jpcc.7b04152
J. Phys. Chem. C XXXX, XXX, XXX−XXX